analytical chemistry

pubs.acs.org/ac Article

Multifunctional Detection of Extracellular Vesicles with Surface Plasmon Resonance Microscopy

Yuting Yang, Chunhui Zhai, Qiang Zeng, Ab Lateef Khan, and Hui Yu*

Cite This: *Anal. Chem.* 2020, 92, 4884−4890 Read Online

ACCESS | Metrics & More | Article Recommendations | Supporting Information

ABSTRACT: Extracellular vesicles (EVs), including exosomes, are promising circulating biomarkers for disease diagnosis. Conventional EVs analysis requires multiple instrumentations to obtain their phenotypic features, which limits its wide applications. Here, we present a plasmonic biosensor technology for multifunctional analysis of EVs. The system is based on a functionalized surface plasmon resonance (SPR) biosensor and an advanced plasmonic microscopy to capture and image EVs at single-particle level. SPR images are processed with a home-developed deep learning algorithm to identify EVs and quantify image intensity automatically. By combining immunosensing and single particle analysis, this approach enables both physical and chemical characterization of EVs. As a proof-of-concept, we applied it to analyze EVs secreted from human lung cancer A549 cell lines. Results show the capabilities in the detection of size, concentration and affinity constant. Due to the single particle imaging and multifunctional analysis capability, we anticipate that this technology will find use in clinical and scientific applications.

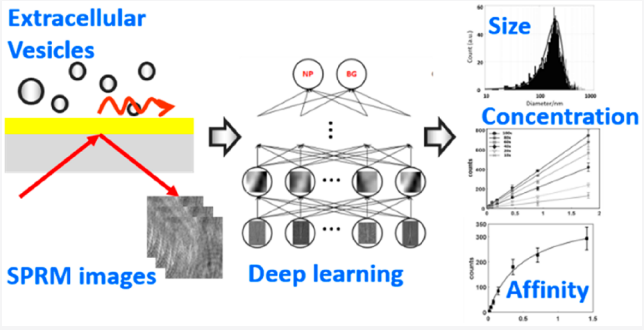

Extracellular vesicles (EVs) are the membrane-enclosed vesicles derived by almost all cell types and present in most bodily fluids, including blood, urine, saliva, breast milk, etc.[1,2] At the time of their discovery, EVs are only thought to be the cargos for cells to eliminate the unneeded compounds.[3] However, more and more focus has been placed on EVs recently, because they are discovered to play an important role in intercellular communications.[4] They can exchange components between cells, varying from proteins, lipids, to nucleic acids, thus maintaining normal cell homeostatic processes or resulting in pathological developments.[4,5] In this context, there is a growing interest in exploring EVs from the biofluid of cancer patients as means of disease diagnosis, as well as progression assessment and therapeutic monitoring. For example, Shao et al. showed that circulating glioblastoma multiform EVs can reflect primary tumor mutations and serve as a predictive metric of treatment-induced changes.[6] Also, different phenotypic features of EVs were found to be associated with diseases. For example, membrane proteins of EVs were identified as biomarkers for various cancer diseases, including melanoma,[7] ovarian,[8,9] pancreatic,[10,11] colorectal,[12] and lung[13] cancers. EVs' concentrations were reported to associate with therapy failure and disease progression in breast cancer patients.[14]

EVs are small but highly heterogeneous in size, ranging from 30 nm to 8 μm.[15] While about 95% of EVs are smaller than 1 μm, including exosomes (30−150 nm in diameter) and microvesicles (200−1000 nm in diameter).[16] Adequate detection and quantitative study of EVs are very difficult due to their heterogeneous size, low refractive index, and polydispersity.[17,18]

Conventional EVs analysis relies on multiple instrumentations to measure both physical features and membrane proteins to allow informative analysis. Electron microscopies (EM), including transmission EM (TEM),[15,19] scanning EM (SEM),[20] and cryo-EM,[21] have enabled ultrahigh resolution imaging of EVs for morphological study, but are limited by complex sample preparation and low throughput. Other approaches including dynamic light scattering (DLS),[22] nanoparticle tracking analysis (NTA),[23,24] and tunable resistance pulse sensing (TRPS)[23] are capable of high throughput analysis of size distribution and/or concentration, but membrane protein information is missing. While conventional protein analysis techniques, such as Western blot,[25] ELISA,[26] and immunolabeling,[27] require complex labeling, surface plasmon resonance (SPR) biosensors[28] allow for label-free and high-throughput mapping of EVs' membrane proteins and provide valuable kinetic information. However, they cannot obtain the physical information due to lack of single-particle sensing ability. Developing a simple detection technique for multifunctional analysis of EVs could thus greatly advance the application of EVs.

Received: October 10, 2019
Accepted: March 5, 2020
Published: March 5, 2020

https://dx.doi.org/10.1021/acs.analchem.9b04622
Anal. Chem. 2020, 92, 4884−4890

Recent advances in single EV imaging and analysis approaches have shed light on the multifunctional detection of EVs. The challenge in single EV analysis lies in the small size down to 30 nm, imposing an extremely high requirement in imaging sensitivity. Lee et al. have made use of single molecule fluorescent microscopy to image single EV, map membrane proteins on its membrane and quantify the size distribution.[29] This method is based on fluorescence labeling, which is less suitable for the dynamic and quantitative study, and requires complex sample preparation. Alternatively, we have developed an interferometric plasmonic microscopy (iPM), which enables the label-free imaging of single exosomes.[30] This approach enables the dynamic analysis of exosomes bound to an antibody-coated metal surface, providing information on the size distribution and membrane proteins. Although powerful, the measurement of concentration and binding constant has not been demonstrated yet in this plasmonic platform.

In this work, we aim to provide a biosensor platform for multifunctional EVs analysis (Figure 1). The proposed methodology is based on single EV imaging with the SPR biosensor and plasmonic microscopy, enabling detection of size distribution, concentration, and affinity of molecular interactions. The sensor surface is modified with antibodies or charged molecules to capture EVs. SPR images were taken, followed by data analysis at the single-EV level using a home-developed deep learning algorithm. EVs isolated from A549-cell line culture medium were used as an example in this work to test the effectiveness.

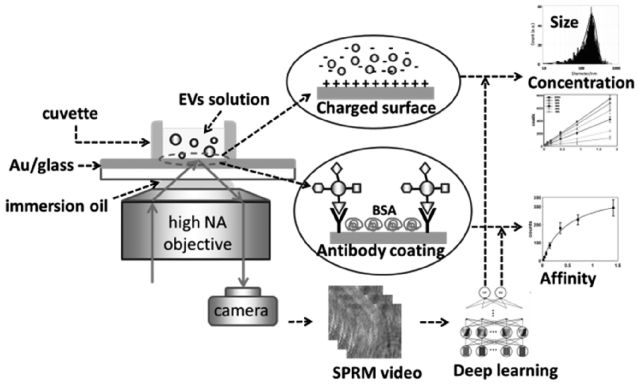

Figure 1. Schematics of EVs detection with SPRM. The SPRM system was based on a high NA objective. For size and concentration detection, the sensor surface is positively charged via SH-PEG-NH_2 modification. For affinity detection, the sensor surface is modified with antibodies at a low covering rate, and BSA is used to block nonspecific bindings. A deep learning algorithm was developed for automatic SPRM image analysis.

MATERIALS AND METHODS

SPR Biosensors. The sensor chips are 12-542-B (Fisher Scientific International, Inc.) glass coverslips coated with 3 nm of chromium and then 47 nm of Au by evaporation. Each chip was rinsed with deionized water and ethanol twice, and blown dry with nitrogen gas. For positive charge modification of the sensor surface to facilitate their binding to the surface, the chip was treated with hydrogen flame and immediately submerged in 10 mM HS-PEG-NH_2 (M_r 10 000 Da; Nanocs) water/ethanol (1:1) solution. After it was left in the solution overnight, the chip was rinsed with deionized water and ethanol, and then blown dry with nitrogen gas.

For antibody coating of the sensor surface, the mouse monoclonal CD 63 antibody (NOVUS) was bound onto the Au surface using a modified *N*-hydroxysuccinimide (NHS) and *N*-ethyl-*N*′-(3-(dimethylamino)propyl)carbodiimide (EDC) reaction.[31] Briefly, the Au surface was treated with hydrogen flame, and then immediately immersed in 1mM 11-Mercaptoundecanoic acid (11-MPA) ethanol solution for carboxylation overnight. The chip was rinsed with PBS buffer, and then activated in 1 mL NHS and EDC mixture (M:M = 1:4) solution for 30 min. Following the activation of carboxyl groups, the chip was incubated in 4 μg/mL of the monoclonal CD63 antibody PBS buffer solution at 37 °C in the dark for 2 h. The chip was rinsed twice with PBS buffer to remove unbound antibody, and 30 μL of BSA solution (1% w/v) was added into the cuvette to block residual activated binding sites for 20 min.

SPRM System and Binding Experiments. The SPRM system used is similar to those described previously.[30] Briefly, the surface plasmons on the metal surface were stimulated via the Kreschmenn configuration (Figure 1). The system was built on an inverted total internal reflection fluorescence microscope (TIRFM) (Olympus IX83) equipped with a high numerical aperture 100× oil immersion objective (N.A. = 1.49). A laser beam at a wavelength of 637 nm (OBIS 637 nm LX FP 100 mW)

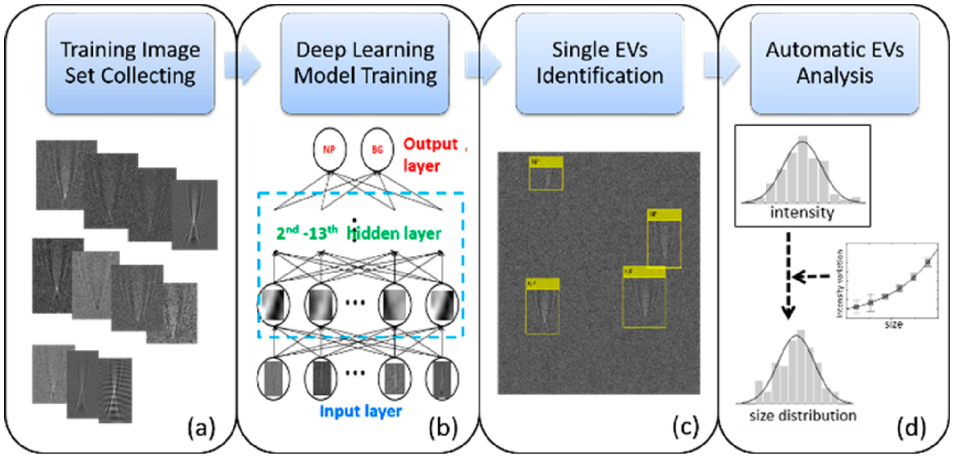

Figure 2. Automatic image processing method for EVs identification. (a) The training set using SPR images of nanoparticles captured under various imaging conditions; (b) Deep learning model training with input layer, hidden layers and output layer (detailed workflow in Figure S1); (c) Typical snapshot during EV detection with deep learning model; (d) Automatic quantitative analysis of EVs.

https://dx.doi.org/10.1021/acs.analchem.9b04622
Anal. Chem. 2020, 92, 4884−4890

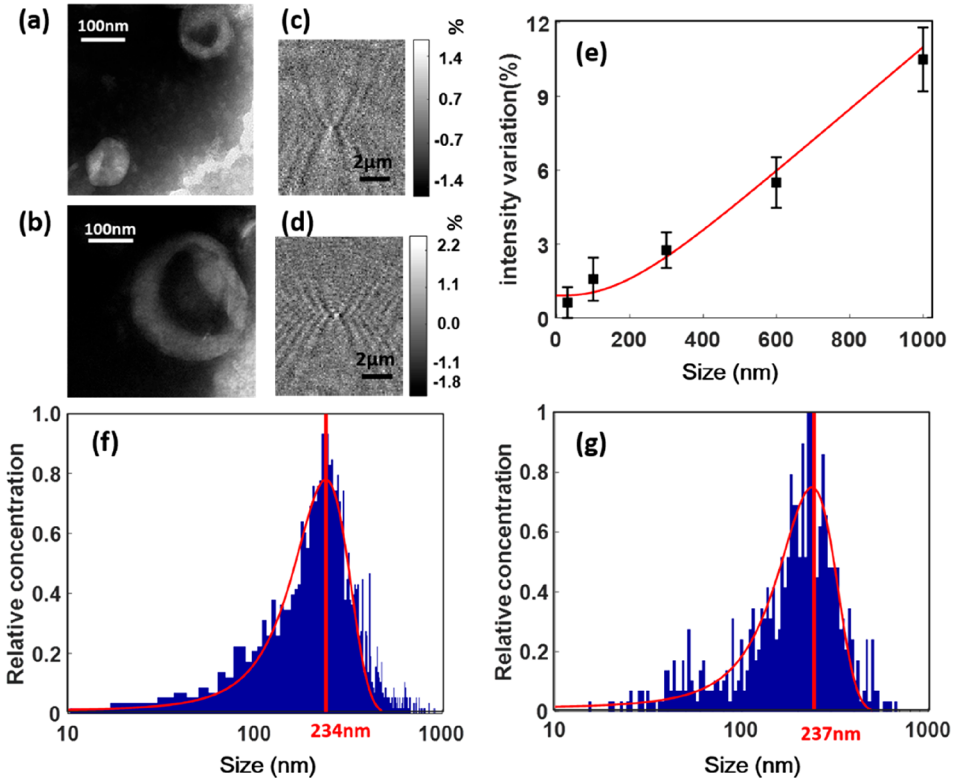

Figure 3. EVs characterization and size measurement. TEM (a, b) and SPRM (c,d) images of single exosome (~80 nm) and microvesicle (~250 nm). (e) Theoretical (red line, fitted with eq 1) and experimental (black markers) calibration curves determined with standardized silica nanoparticles with sizes of 30 nm, 100 nm, 300 nm, 600 nm, and 1um. Size measurement of EVs with SPRM (f) and NTA (g), and the red curve is fitted with a Gaussian model. Mean values were located at 234 and 237 nm, respectively.

was collimated, and illuminated the sensor chip at a highly inclined incident angle close to SPR dip angle. The reflective light, together with the scattering light, was collected and sensed by a CMOS camera (Prime TM; Photometrics). A motorized XY stage (Ludl Electronic Products, Ltd.) was incorporated on the microscope to translate the sensor chip.

For sample holding, we used a homemade polydimethylsiloxane (PDMS) cuvette with a total volume of ~35 μL. For binding experiments, 2 μL PBS buffer was first added into the cuvette, and the camera and light source parameters were tuned for best recording performance. An area of 600 × 600 pixels (full field of view: 39 × 39 μm^2) with uniform illumination was selected as the region of interest for detection. Ten μL samples were pipetted into the cuvette, and images were immediately recorded at a frame rate of 100 fps.

Offline Automatic Image Processing. Images recorded by CMOS camera were analyzed offline with MATLAB R2017a (MathWorks). Running average with n = 30 frames was first applied to minimize the shot noise. Then differential images between two adjacent averaged images were calculated to remove the static background, leaving only images of bounded EVs. Automatic discriminating the single particle image from the noisy background is very challenging as the signal noise ratio is limited for nanoscale biological samples, and researchers have tried to make use of image processing techniques including filtering, thresholding, blob recognition, seed growing, etc.[32] These traditional methods failed to be widely adopted due to poor robustness, as they required a lot of preset parameters.

To realize automatic and robust EV identification from SPR images, we turned to deep learning algorithm (Figure 2). We used an 13-layer region-based convolutional neural network (CNN)[33] with the Neural Network Toolbox in MATLAB 2017a, and the detailed workflow can be found in Figure S1 (Supporting Information). The region proposals were empirically generated as 80 × 120 pixels' regions with certain foreground, determined by simple binarization. The training set (Figure 2a) was composed of more than 5000 SRPM images of silica nanoparticles acquired under different imaging conditions (incident angle and focus) with nanoparticles of various sizes (30, 100, 300, 600, 1000 nm). After training, the deep learning model was used to automatically identify particles from the SRPM images, and record information in location, intensity, and numbers. This information was later used for size determination by interpolating the intensity with a calibration curve, and for concentration and binding affinity analysis by EVs count over time.

Silica Nanoparticle Calibration. Silica nanoparticles (purchased from MikroNano Partikel GmbH) with sizes of 30 nm, 100 nm, 300 nm, 600 nm, and 1 μm were used to cover the full size range of our EV samples. Raw silica nanoparticle samples were diluted with PBS at 1:1000 vol/vol, and ultrasonicated for 30 min for redispersion. Then 10 μL of nanoparticle solution was injected into the cuvette on a positive-charge modified sensor surface, and images were recorded immediately for 2 min. Each experiment was repeated three times.

The intensities of individual silica nanoparticles were measured by SPRM as the mean value of a 3 × 3 pixels region of interest centered at the largest intensity pixel. To compensate for the nonuniformity of incident light intensity distribution, particle induced intensity change was described as the ratio over background intensity of the region of interest in SPRM image before binding. Histograms of intensity distribution at different

https://dx.doi.org/10.1021/acs.analchem.9b04622
Anal. Chem. 2020, 92, 4884−4890

silica nanoparticle sizes were statistically calculated, and the mean value is determined with a Gaussian model. The particle induced intensity change at different sizes were fitting following the theoretical model:[34]

$$I = k\int_0^{2\pi} \pi(2rz - z^2)e^{-z/l}dz \quad (1)$$

where k is a constant (the fitting parameter), z is the distance above the sensor chip surface, r is radius of the particle, and l is the decay constant of the evanescent field, which is approximately 200 nm.

Cell Culture and EVs Isolation. Human lung cancer A549 cells (American Type Culture Collection, ATCC) were maintained in Dulbeco's modified essential medium (HyClone; GE Healthcare), supplemented with EV-depleted 10% fetal bovine serum (FBS) (Invitrogen, Thermo Fisher Scientific) and 1% (v/v) penicillin-streptomycin (Invitrogen, Thermo Fisher Scientific). The cells were incubated in a humidified incubator (Thermo Fisher Scientific) at 37 °C with 5% CO2 and used at passage 2−20. The cell culture medium was collected after 48 h when the cells were 90% confluent with a viability of >95% (Trypan blue).

Cell culture media (200 mL) was first centrifuged at 2000g for 30 min to remove the cells. The supernatant was further centrifuged at 10 000g for 30 min to remove cell debris. After filtering using a 1 μm membrane filter (Millipore), the supernatant was further ultracentrifuged at 100 000g for 90 min at 4 °C to retain the precipitated pellets of extracellular vesicles (EVs). The EV pellets were washed with 30 mL phosphate buffered saline (PBS) once, and precipitated by a second ultracentrifugation at 100 000g for 90 min at 4 °C, and then supernatant was discarded. The purified EVs were redispersed in 200 μL of 1× PBS solution (pH 7.4) for use.

The size and concentration of isolated EV samples were determined with nanoparticle tracking analysis. The EV sample was diluted (1:100000) in sterile PBS and analyzed (1 mL) with a Nanosight NS300 (Malvern Panalytical, Westborough, MA). For transmission electron microscopy (TEM) imaging, EVs were fixed in 4% paraformaldehyde (1:1) at room temperature (2 min), placed (8 μL) on carbon-Formvar-coated copper grids (300 mesh), and blotted. Water (8 μL) was added to the samples that were then blotted, and 2% aqueous uranyl acetate (8 μL) was placed on the grid (2 min) and blotted. The grids were examined with a transmission electron microscope (Talos L120C G2, 120 kV, Thermo Fisher Scientific).

RESULTS AND DISCUSSION

SPRM Imaging of Single EVs. After EVs isolation from cell culture medium, we examined the sample with TEM to check the morphology. Figure 3a and b shows typical TEM images of an exosome (~80 nm) and a microvesicle (~250 nm), with typical "teapot" and round shapes, respectively. Figure 3c and d show the typical SPRM images recorded during the binding onto a positive charge modified Au surface, showing similar shapes but different intensity. We also used standardized silica nanoparticles as a reference to calibrate the system, which has a refractive index of 1.46, close to that of EVs. This method has been well studied and widely used in size measurement with SPRM.[30,34] We monitored the binding process of single silica nanoparticles onto positive-charge modified Au surface, and clearly observed single silica nanoparticles ranging from 30 to 1000 nm (Figure S2). This thus confirms the capability in full size range analysis of the EVs. A calibration curve was established as the intensity change induced by single nanoparticle at different sizes (Figure 3e), and fitted following the theoretical model in eq 1.

Automatic Detection of EVs with Deep Learning Algorithms. We developed a deep learning algorithm (Figure 2) to automatically identify EVs from SPRM images. The model was trained with a large number of SPRM images of silica nanoparticles of different sizes recorded at different imaging conditions. After that, it was applied to automatically identify the EVs from the SPRM images. Figure 2c shows the typical recognition results in SPRM images of multiple EVs, which accurately detected observable EVs in one frame. Based on the statistical analysis, the accuracy, defined as correctly identified particle number divided by total particle number, reached 89.78% in training data, and 85.26% in testing data, as verified by visual check. Most failed detection happened to those located close to the margins of images, or the overlapping of multiple EVs. The influence by overlapping of multiple EVs could be minimized by a careful tuning of sample concentrations. The whole processing time for a video containing 10 000 images was around 5 min. The automatic processing thus enables the analysis of a large number of EVs for statistical analysis in a much shorter time than manual selection.

We note that the automatic detection and quantification of nanoparticles from the image is a key step in nanoparticle analysis. Due to the unique pattern in SPRM images, unique approaches were required to enable robust and accurate detection. The image processing algorithms that we previously developed could help remove the "tail" shape pattern and restore the image as a bright spot;[35] however, the deconvolution during processing would introduce unwanted background noises, and make the conventional thresholding detection technique fail. At the meantime, the "tail" patterns could actually assist visual or automatic detection as unique features, as background noise would not show similar patterns. But since the tail patterns differ with the focus change and incident angle, it imposes difficulties in the automatic EV recognition using simple template matching. Our deep learning technology thus provided a better solution to this problem.

Size Measurement. The intensity of SPRM image of a nanoparticle is dependent on its size, which has been extensively used in nanoparticle analysis. In our experiment, the surface was first modified with positive charges to allow strong binding of EVs, as the net charge of EVs' membrane is negative. The raw concentration of EVs as determined by NTA was ~2.5×10^{12}/mL. We then recorded the SPRM video during the binding process (Movie S1) for 100 s, followed by the automatic data processing to quantify the intensity distribution of EVs detected in each frame. Interpolating the intensity onto the calibration curve yields the estimated size of EVs sample. The size distribution of EVs was calculated and fitted by a standard Gaussian model (Figure 3f and g). Note that the fitting curve appears asymmetrical due to the logarithmic label on x-axis. The experiments were repeated in triplicate, and the mean value was located at 234 ± 49 nm, which is similar to that of 237 ± 36 nm determined with NTA (Figure 3g). The percentage ratio of exosome (<150 nm) and other microvesicle (150 nm ~1um) is 12.5% and 87.5%, respectively. In the microvesicle subset, approximately 80% are vesicles with the size below 400 nm. Previously reported plasmonic biosensors for EVs analysis depends on averaged signal from multiple EVs, and did not resolve signal from single EVs, losing information in size distribution.

https://dx.doi.org/10.1021/acs.analchem.9b04622
Anal. Chem. 2020, 92, 4884−4890

Concentration Detection. As the number of detected EVs depends on the diffusion of EVs onto the sensor surface, it can be used to estimate the concentration of EV samples. Here we dilute the EVs samples within $1.8 \times 10^8 \sim 1.8 \times 10^{10}$/mL as confirmed by NTA, which covers the common concentration range of EVs samples in blood.[36] Figure 4a plots the number of EVs detected on a positively charged sensor surface in the 100 s recording, constructed by counting the EVs frame by frame. We observed a continuously increasing number of EVs binding to the sensor surface, with different binding rate depending on the concentration. Figure 4b shows the relationship between detected EVs' count and raw concentrations in the sample determined at different time after sample addition. The blue dashed line indicates the low background noise tested with blank PBS solution without EVs. Good linearity is observed in the range of 10^8–10^{10} /mL with a fast detection time as short as 10 s. A longer detection time allows for more EVs to be analyzed, resulting in a larger sensitivity (slope). The single EV analysis capability thus offers a simple and rapid way of measuring EVs' concentrations.

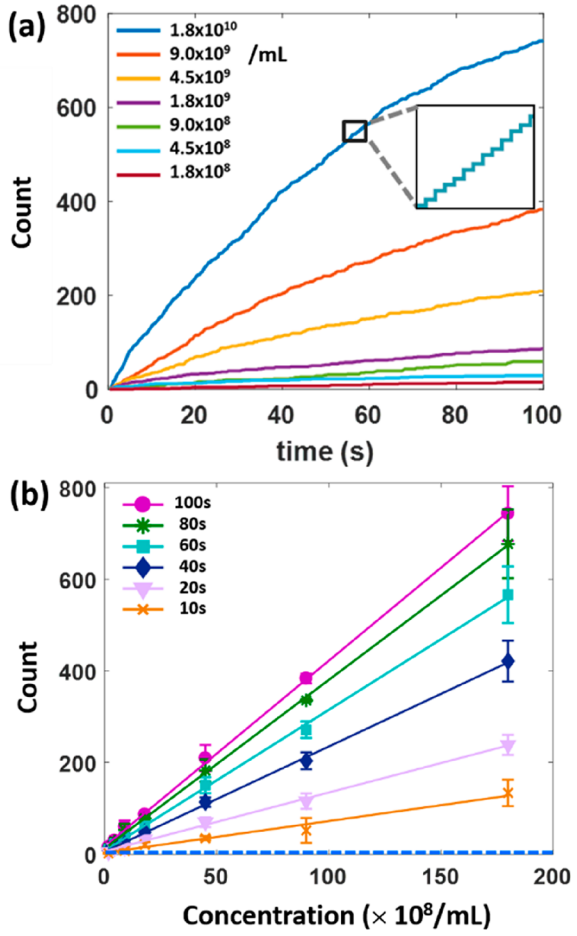

Figure 4. EVs' concentration detection. (a) EVs count vs binding time at different EVs' concentrations. The subset shows the stepwise counting at single EV accuracy. (b) EVs count vs EVs' concentrations at different assay time, showing a linear relationship in as short as 10 s. The blue dashed line indicates the noise level determined as the count in blank solution. $n = 3$ for statistical analysis.

Specific Binding Between EVs and CD63-Antibody. Modifying the SPR sensor surface with different biorecognition molecules would allow specific study of membrane proteins of EVs. Due to the sensitivity limitation, conventional SPR measures the average signal from a large number of analyte molecules, and thus requires high functionalization efficiency of the sensor surface. Also, conventional SPR uses a constant flowing sample during binding process to avoid analyte depletion, requiring a large sample volume. However, for EVs, a practical limitation is in the obtainable sample concentration and volume. SPRM allows for single EV imaging, and thus low functionalization efficiency of the sensor surface minimized the required number of EVs to reach equilibrium without sample depletion. Thus, we modified the surface with a low density of CD63 antibody, a type III lysosomal membrane protein abundant in and characteristic of EVs, to show the capability in specific detection of CD63-positive EVs. Note that we use a 4 μg/mL antibody solution for the surface coating to achieve extremely low functionalization efficiency, far from the commonly used 50–100 μg/mL range for high functionalization efficiency.

The EVs solution is diluted from the raw concentration of 2.5×10^{12} /mL (4.15 nM), and converted into molar concentration for easier interpretation with binding constant. As the specific binding between EVs and antibody is reversible, we observe both binding and unbinding events (Figure 5a). As we measure the differential image between consecutive frames, the SPRM images of binding (red) and unbinding events (green) showed opposite contrast. We then statistically calculate the count of binding, unbinding, and the net events during the binding process, as shown in Figure 5b for the EVs' concentration of 0.04 nM. At the beginning, mainly binding events were observed (Movie S2), and the EVs' count increased rapidly. After 500 s, both binding and unbinding events were detected (Movie S3), and the EVs' count reached a plateau, indicating the equilibrium status.

Figure 5c shows the net count of EVs binding to the antibody coated surface in 600 s at different EVs' concentrations. After 500–600 s, the binding reaches equilibrium as all net count of EVs did not increase. The affinity, described as the equilibrium dissociation constant K_D, is fitted by nonlinear regression using the Langmuir binding isotherm:

$$N_{EV} = N_{max}\left(\frac{C_{EV}}{K_D + C_{EV}}\right) \quad (2)$$

where N_{EV} is the number of EVs counted at equilibrium status, C_{EV} is the EVs' sample concentration, and N_{max} is the maximum binding capacity. N_{max} and K_D were fitted according to N_{EV} at equilibrium as a function of analyte concentration C_{EV}. The observed K_D is ~0.79 ± 0.12 nM, which is close to that of individual antibody–antigen binding (1 nM). The fitted N_{max} is ~786, meaning a maximum number of 786 binding sites in the full field of view (39 μm × 39 μm). Thus, the average distance between antibody moleculescould be estimated to be $\frac{39}{\sqrt{786}} = 1.39\mu$m, indicating an extremely low coating efficiency as expected.

In the nanoplasmonic biosensors reported before, binding constant could be measured by the resonance angle shift induced by the EVs, observing a binding constant of ~36 pM[8]. In this work, we have observed more than an order of magnitude higher K_D value that is closer to individual antibody–antigen binding. We attribute it to the less likelihood of multiple antigen–antibody interactions on one EV, due to the low functionalization efficiency. Wang et al.[37] has recently reported

https://dx.doi.org/10.1021/acs.analchem.9b04622
Anal. Chem. 2020, 92, 4884–4890

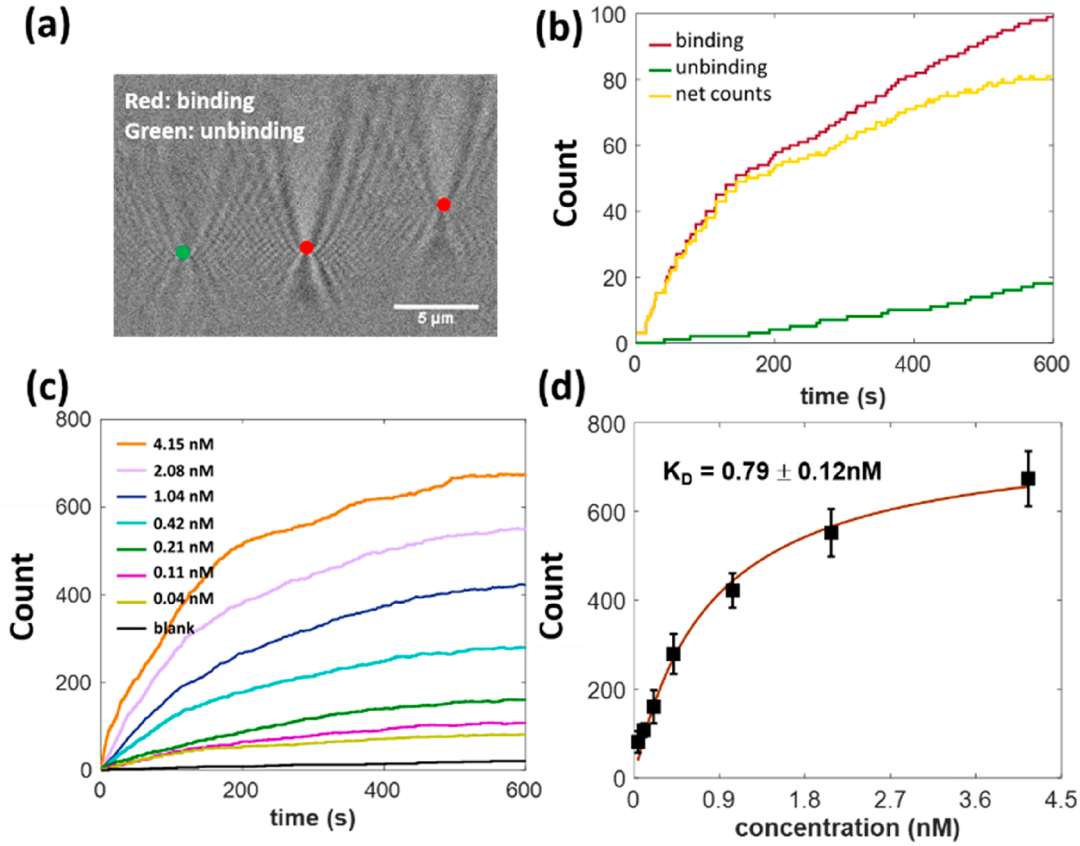

Figure 5. Detecting specific binding between EVs and CD63 antibody. (a) Typical snapshots from the video of EVs' on CD63 antibody coated sensor surface, showing both binding (red) and unbinding (green) events recorded. (b) EVs count showing total binding (blue), unbinding (red), and net (binding-unbinding, black) binding events. (c) Net EVs count vs binding time at different EVs' concentrations; (d) Net EVs count vs EVs' concentrations at 600 s, fitted with the Langmuir binding isotherm. n = 3 for statistical analysis.

that multiple antigen−antibody interactions are highly dependent on the surface modification efficiency, which clearly support our results. They also showed that the Brownian motion would induce an intensity change during binding process, which we did observe as well. It prevents us to accurately acquire the EVs' sizes, and thus a detailed analysis of binding affinity difference between EVs of different sizes was demonstrated in this work.

CONCLUSIONS

In this work, we demonstrated surface plasmon resonance biosensors integrated with plasmonic microscopy for multifunctional detection of extracellular vesicles. Information of physical properties, including size distribution and concentration, as well as biochemical properties of membrane proteins could be measured by imaging the process of EVs binding onto sensor surfaces. Binding affinity between antibody and EV interaction could be deduced by real-time monitoring of the number of EVs binding onto the antibody-coated surface. The proposed biosensor thus provides a simple yet effective way for EVs study.

ASSOCIATED CONTENT

Supporting Information

The Supporting Information is available free of charge at https://pubs.acs.org/doi/10.1021/acs.analchem.9b04622.

Workflow of the deep learning algorithms; typical SPRM images of silica nanoparticles (PDF)

Videos of extracellular vesicles binding and unbinding events, SPRM video (AVI)

Binding events (AVI)

Binding and unbinding events (AVI)

AUTHOR INFORMATION

Corresponding Author

Hui Yu − *School of Biomedical Engineering, Institute for Personalized Medicine, Shanghai Jiao Tong University, Shanghai 200030, China*; orcid.org/0000-0002-6927-4451; Email: hui.yu@sjtu.edu.cn

Authors

Yuting Yang − *School of Biomedical Engineering, Institute for Personalized Medicine, Shanghai Jiao Tong University, Shanghai 200030, China*

Chunhui Zhai − *School of Biomedical Engineering, Institute for Personalized Medicine, Shanghai Jiao Tong University, Shanghai 200030, China*

Qiang Zeng − *School of Biomedical Engineering, Institute for Personalized Medicine, Shanghai Jiao Tong University, Shanghai 200030, China*

Ab Lateef Khan − *School of Biomedical Engineering, Institute for Personalized Medicine, Shanghai Jiao Tong University, Shanghai 200030, China*; orcid.org/0000-0001-6220-2992

Complete contact information is available at: https://pubs.acs.org/10.1021/acs.analchem.9b04622

Notes

The authors declare no competing financial interest.

https://dx.doi.org/10.1021/acs.analchem.9b04622
Anal. Chem. 2020, 92, 4884−4890

■ ACKNOWLEDGMENTS

This work was supported by the National Natural Science Foundation of China (Grants 61901257 and 61805136), the Shanghai Pujiang Program (Grant 18PJ1406400), and the China Postdoctoral Science Foundation (Grant 2018M642025) for financial support. The authors declare no competing financial interest.

■ REFERENCES

(1) Robbins, P. D.; Morelli, A. E. *Nat. Rev. Immunol.* **2014**, *14*, 195.
(2) Raposo, G.; Stoorvogel, W. *J. Cell Biol.* **2013**, *200* (4), 373−383.
(3) Johnstone, R. M.; Adam, M.; Hammond, J.; Orr, L.; Turbide, C. *J. Biol. Chem.* **1987**, *262* (19), 9412−9420.
(4) Yáñez-Mó, M.; Siljander, P. R.-M.; Andreu, Z.; Bedina Zavec, A.; Borràs, F. E.; Buzas, E. I.; Buzas, K.; Casal, E.; Cappello, F.; Carvalho, J. *J. Extracell. Vesicles* **2015**, *4* (1), 27066.
(5) van Niel, G.; D'Angelo, G.; Raposo, G. *Nat. Rev. Mol. Cell Biol.* **2018**, *19*, 213.
(6) Shao, H.; Chung, J.; Balaj, L.; Charest, A.; Bigner, D. D.; Carter, B. S.; Hochberg, F. H.; Breakefield, X. O.; Weissleder, R.; Lee, H. *Nat. Med.* **2012**, *18* (12), 1835.
(7) Logozzi, M.; De Milito, A.; Lugini, L.; Borghi, M.; Calabrò, L.; Spada, M.; Perdicchio, M.; Marino, M. L.; Federici, C.; Iessi, E.; Brambilla, D.; Venturi, G.; Lozupone, F.; Santinami, M.; Huber, V.; Maio, M.; Rivoltini, L.; Fais, S. *PLoS One* **2009**, *4* (4), No. e5219.
(8) Im, H.; Shao, H.; Park, Y. I.; Peterson, V. M.; Castro, C. M.; Weissleder, R.; Lee, H. *Nat. Biotechnol.* **2014**, *32* (5), 490.
(9) Zhao, Z.; Yang, Y.; Zeng, Y.; He, M. *Lab Chip* **2016**, *16* (3), 489−496.
(10) Liang, K.; Liu, F.; Fan, J.; Sun, D.; Liu, C.; Lyon, C. J.; Bernard, D. W.; Li, Y.; Yokoi, K.; Katz, M. H. *Nature biomedical engineering* **2017**, *1* (4), 0021.
(11) Melo, S. A.; Luecke, L. B.; Kahlert, C.; Fernandez, A. F.; Gammon, S. T.; Kaye, J.; LeBleu, V. S.; Mittendorf, E. A.; Weitz, J.; Rahbari, N. *Nature* **2015**, *523* (7559), 177.
(12) Yoshioka, Y.; Kosaka, N.; Konishi, Y.; Ohta, H.; Okamoto, H.; Sonoda, H.; Nonaka, R.; Yamamoto, H.; Ishii, H.; Mori, M. *Nat. Commun.* **2014**, *5*, 3591.
(13) Jakobsen, K. R.; Paulsen, B. S.; Bæk, R.; Varming, K.; Sorensen, B. S.; Jørgensen, M. M. *J. Extracell. Vesicles* **2015**, *4* (1), 26659.
(14) König, L.; Kasimir-Bauer, S.; Bittner, A.-K.; Hoffmann, O.; Wagner, B.; Santos Manvailer, L. F.; Kimmig, R.; Horn, P. A.; Rebmann, V. *Oncoimmunology* **2018**, *7* (1), No. e1376153.
(15) Arraud, N.; Linares, R.; Tan, S.; Gounou, C.; Pasquet, J. M.; Mornet, S.; Brisson, A. R. *J. Thromb. Haemostasis* **2014**, *12* (5), 614−627.
(16) Colombo, M.; Raposo, G.; Théry, C. *Annu. Rev. Cell Dev. Biol.* **2014**, *30* (1), 255−289.
(17) Lozano-Andrés, E.; Libregts, S. F.; Royo, F.; López, S. M.; López-Martín, S.; Valés, M.; Reyburn, H. T.; Wauben, M. H.; Falcón-Pérez, J. M.; Yáñez-Mó, M. *J. Extracell. Vesicles* **2018**, *7*, 20−20.
(18) Kowal, J.; Arras, G.; Colombo, M.; Jouve, M.; Morath, J. P.; Primdal-Bengtson, B.; Dingli, F.; Loew, D.; Tkach, M.; Théry, C. *Proc. Natl. Acad. Sci. U. S. A.* **2016**, *113* (8), E968−E977.
(19) Rikkert, L.; Nieuwland, R.; Terstappen, L.; Coumans, F. *J. Extracell. Vesicles* **2019**, *8* (1), 1555419.
(20) Nanou, A.; Crespo, M.; Flohr, P.; De Bono, J.; Terstappen, L. *Cancers* **2018**, *10* (11), 416.
(21) Yuana, Y.; Koning, R. I.; Kuil, M. E.; Rensen, P. C.; Koster, A. J.; Bertina, R. M.; Osanto, S. *J. Extracell. Vesicles* **2013**, *2* (1), 21494.
(22) Palmieri, V.; Lucchetti, D.; Gatto, I.; Maiorana, A.; Marcantoni, M.; Maulucci, G.; Papi, M.; Pola, R.; De Spirito, M.; Sgambato, A. *J. Nanopart. Res.* **2014**, *16* (9), 2583.
(23) Van der Pol, E.; Coumans, F.; Grootemaat, A.; Gardiner, C.; Sargent, I.; Harrison, P.; Sturk, A.; Van Leeuwen, T.; Nieuwland, R. *J. Thromb. Haemostasis* **2014**, *12* (7), 1182−1192.
(24) Gleadle, J.; McNicholas, K.; Li, J.; Michael, M.; Rojas-Canales, D. *J. Am. Soc. Nephrol.* **2018**, *29* (6), 1784−1784.
(25) Rafols, F. X. G.; Corbett, G. T.; Cha, D. J.; Mustapic, M.; Liu, W.; Mengel, D.; Chen, Z.; Aikawa, E.; Young-Pearse, T.; Kapogiannis, D. *J. Extracell. Vesicles* **2018**, *7*, 176−177.
(26) Moon, P.-G.; Lee, J.-E.; Cho, Y.-E.; Lee, S. J.; Chae, Y. S.; Jung, J. H.; Kim, I.-S.; Park, H. Y.; Baek, M.-C. *Oncotarget* **2016**, *7* (26), 40189.
(27) Thane, K. E.; Davis, A. M.; Hoffman, A. M. *Sci. Rep.* **2019**, *9* (1), 1−13.
(28) Rupert, D. L. M.; Lässer, C.; Eldh, M.; Block, S.; Zhdanov, V. P.; Lotvall, J. O.; Bally, M.; Höök, F. *Anal. Chem.* **2014**, *86* (12), 5929−5936.
(29) Lee, K.; Fraser, K.; Ghaddar, B.; Yang, K.; Kim, E.; Balaj, L.; Chiocca, E. A.; Breakefield, X. O.; Lee, H.; Weissleder, R. *ACS Nano* **2018**, *12* (1), 494−503.
(30) Yang, Y.; Shen, G.; Wang, H.; Li, H.; Zhang, T.; Tao, N.; Ding, X.; Yu, H. *Proc. Natl. Acad. Sci. U. S. A.* **2018**, *115* (41), 10275−10280.
(31) Sam, S.; Touahir, L.; Salvador Andresa, J.; Allongue, P.; Chazalviel, J.-N.; Gouget-Laemmel, A.; Henry de Villeneuve, C.; Moraillon, A.; Ozanam, F.; Gabouze, N. *Langmuir* **2010**, *26* (2), 809−814.
(32) Sidorenko, I.; Nizamov, S.; Hergenröder, R.; Zybin, A.; Kuzmichev, A.; Kiwull, B.; Niessner, R.; Mirsky, V. M. *Microchim. Acta* **2016**, *183* (1), 101−109.
(33) Girshick, R.; Donahue, J.; Darrell, T.; Malik, J. *Proceedings of the IEEE conference on computer vision and pattern recognition* **2014**, 580−587.
(34) Wang, S.; Shan, X.; Patel, U.; Huang, X.; Lu, J.; Li, J.; Tao, N. *Proc. Natl. Acad. Sci. U. S. A.* **2010**, *107* (37), 16028−16032.
(35) Yu, H.; Shan, X.; Wang, S.; Tao, N. *Anal. Chem.* **2017**, *89* (5), 2704−2707.
(36) Coumans, F. A. W.; van der Pol, E.; Böing, A. N.; Hajji, N.; Sturk, G.; van Leeuwen, T. G.; Nieuwland, R. *J. Extracell. Vesicles* **2014**, *3* (1), 25922.
(37) Wang, H.; Tang, Z.; Wang, Y.; Ma, G.; Tao, N. *J. Am. Chem. Soc.* **2019**, *141* (40), 16071−16078.

https://dx.doi.org/10.1021/acs.analchem.9b04622
Anal. Chem. 2020, 92, 4884−4890